Supplement for

A Novel Pathway of Atmospheric Sulfate Formation Through Carbonate Radical

Yangyang Liu[1,2], Yue Deng[1,2], Jiarong Liu[3], Xiaozhong Fang[1], Tao Wang[1], Kejian Li[1], Kedong Gong[1], Aziz U. Bacha[1], Iqra Nabi[1], Xiuhui Zhang[3], Christian George[4], and Liwu Zhang[1,2]

[1]Shanghai Key Laboratory of Atmospheric Particle Pollution and Prevention, Department of Environmental Science and Engineering, Fudan University, Shanghai, 200433, P. R. China.

[2]Shanghai Institute of Pollution Control and Ecological Security, Shanghai, 200092, Peoples' Republic of China.

[3]Key Laboratory of Cluster Science, Ministry of Education of China, School of Chemistry and Chemical Engineering, Beijing Institute of Technology, Beijing 100081, P. R. China

[4]Univ. Lyon, Université Claude Bernard Lyon 1, CNRS, IRCELYON, F-69626, Villeurbanne, France.

Correspondence to: Liwu Zhang (zhanglw@fudan.edu.cn)

Supplement Text 1

Characterization of mineral dust proxies TiO_2 and $CaCO_3$. Commercial Degussa TiO_2 dust particles after heat pretreatment were characterized by X-ray diffraction and BET measurements. The result (Fig. S1A) confirms the existence of the anatase phase and rutile phase in TiO_2, with a surface area of 49.9 m^2 g^{-1}. For ground TiO_2-$CaCO_3$ particles, the XRD pattern shows the feature assembly of ground TiO_2 and $CaCO_3$ particles (Fig. S1B). In Fig. S1C, anatase crystal with tetragonal structure and rutile crystal of P4/mnm space group was further probed by Raman spectra, with several active optical phonon modes at the vicinity of 139, 189, 387, 508, and 628 cm^{-1}, which are in good agreement with previous studies (Su et al., 2008;Balachandran and Eror, 1982).

Supplement Text 2

Measurements of sulfate formation on mineral dust proxies TiO_2 after exposure to SO_2 in the presence and absence of CO_2 upon irradiation. 25 mg of TiO_2 after heat pretreatment (400 ℃ for 5 h) was installed into the homemade quartz chamber (d= 5.5 cm, H=1.2 cm, and actual volume= 20 cm^3, one inlet and one outlet). Subsequently, particles were further pretreated under simulative solar irradiation for 1h with dry air gas flow (100 mL min^{-1}) to remove most of the carbonaceous residuals and impurities that remain on particle surfaces. Afterward, a gas flow of (7.37×10^{13} molecule cm^{-3} SO_2) /N_2+O_2 or (9.83×10^{15} molecule cm^{-3} CO_2) + (7.37×10^{13} molecule cm^{-3} SO_2) /N_2+O_2 were introduced into the reaction chamber for 3h under irradiation (RH= 30 % and Light intensity (I) = 30 mW cm^{-2}) and 15 mg of the particles were then taken out and dissolved into the 4 mL leaching solution (3 % vol. formaldehyde), shaken by using an oscillator for 5 min, and the derived extracting solution was filtered with 0.22 μm PTFE membrane, followed by sending it into IC for sulfate ion measurements.

Supplement Text 3

Preparation for clay and dust membranes and investigation of sulfate formation on those authentic particles during the daytime and nighttime. Each particle suspension ATD (2.5 mg~0.5 mL), IMt-2 (10 mg~ 0.5 mL) and K-GA (10 mg~ 0.5 mL) were first dispersed into water through ultrasonic bath for 5 min. After that, sample suspensions were transformed onto the cleansed round quartz films (d= 2 cm) using a pipette and subsequently sent to the infrared drying oven for 10 min to prepare dust membranes. Once samples were taken out from the oven, they were quickly sealed into a desiccator and cooled down to room temperature before starting experiments. A membrane sample was then mounted at the center of reaction chamber (the upper half made of quartz and the lower half made of Teflon). Before each set of experiment, a gas flow (dry air) of 300 mL min^{-1} was introduced to the chamber that was installed with a prepared membrane sample for 5 min. Afterward, samples were exposed to 4.91×10^{14} molecule cm^{-3} SO_2 (2.46×10^{18} CO_2 when necessary) /N_2+O_2 mixture in the absence and presence of irradiation (Light intensity (I) = 30 mW cm^{-2}) for 15 min before the sample were transferred to a beaker (Scale= 10 mL) with 2 mL of 2 % vol. isopropanol leaching solution, extracting ions in the ultrasonic tank for 5 min using 0.22 μm PTFE membrane filter, followed by sending the sample into IC. Noting that dust and clay particles possess a considerable amount of sulfate ion background, we thus measured the background ions for each batch of synthesized dust particle membranes following the procedures described above. All data demonstrated in Fig. S10 were obtained after subtraction of background ions.

Supplement Text 4

Determination of reaction order. Calculation of uptake coefficient is the way to describe the reaction efficiency of gas/surface interactions. Before that, sulfate formation rates as a function of SO_2 concentration were initially determined to verify its reaction order in the selected concentration range (Fig. S9 A-E), which is a crucial step to give a credible estimation of SO_2 uptake coefficient. Based on a prior study (Shang et al., 2010), SO_2 uptake on particle surfaces depends on the SO_2 concentrations and active sites, which thus could be described by the following equation (Eq. **S1**):

$$\frac{d[SO_4^{2-}]}{dt}=k[SO_2]^m[CO_2]^l[TiO_2]^n[H_2O]^p \qquad \textbf{[S1]}$$

where $[SO_4^{2-}]$ refers to the sulfate concentration on TiO_2 surfaces, $[SO_2]$($[CO_2]$) to SO_2 (CO_2) gas concentration employed in the system, $[TiO_2]$ to the concentration of active sites on the TiO_2 particle surfaces, and $[H_2O]$ represents for surface water concentration, and m, l, n, and p are the reaction orders of corresponding species. Clearly, the steady growth of sulfate on TiO_2 particles in the presence of 9.83×10^{15} molecules cm^{-3} CO_2 made a clear indication (panel A-E) that the decrease in surface active sites is negligible. Meanwhile, mass flow controllers provide stable gas flow and maintain the constant concentrations of humidified air and CO_2, which allow us to simplify the Eq. **S1** to Eq. **S2** through a logarithm function.

$$\lg\frac{d[SO_4^{2-}]}{dt}= \lg k+ m\lg[SO_2]+ C \qquad \textbf{[S2]}$$

where C stands for $Ilg[TiO_2]+ nlg[TiO_2]+ plg[H_2O]$, and $[SO_2]$ for the concentration of SO_2 where particles are exposed. We then plotted the sulfate formation rate against exposed SO_2 concentration. Linear fitting analysis for those points resulted in 1.13 order for the reaction, with $R^2\approx 0.99$ (Fig. S9 F). So far, 400 ppb is the lowest concentration that we are able to apply for the uptake measurements due to the limitation of the current experimental setup. The prior work has demonstrated that atmospheric SO_2 concentration reaches up to 40 ppb (Franchin et al., 2015). We note that a difference of nearly a factor of 10 remains for the SO_2 concentration employed in laboratory studies and that measured in field observations. Nevertheless, we have already verified its pseudo-first-order kinetic in the wide range of 400-20000 ppb. This leads us to assume that uptake coefficients estimated under ppm level remain valid, and those datasets derived from laboratory chambers are able to be generalized to the atmosphere condition.

Supplement Text 5

Methodology for uptake coefficient estimation. The reaction uptake coefficient was estimated by the following Eqs. **S3-5**, as suggested by the previous work (Kong et al., 2014):

$$\gamma=\frac{d[SO_4^{2-}]/dt}{Z} \quad \textbf{[S3]}$$

$$Z=\frac{1}{4}\times A_s\times[SO_2]\times v \quad \textbf{[S4]}$$

$$v=\sqrt{8RT/\pi M_{SO2}} \quad \textbf{[S5]}$$

where ν is the mean molecular velocity of SO_2, A_s the effective sample surface, R the gas constant, T the temperature, M_{SO2} the molecular weight of SO_2, and a total number of surface collisions per unit time (*Z*). To be precise, the formation rates ($d[SO_4^{2-}]/dt$) in the equation were determined by IC measurements, followed by a conversion factor calculation through linear regression analysis for the integrated absorbance of sulfate bands and corresponding sulfate concentrations. By employing this method, a conversion factor of f = 6.34×10^{15} ions integrated absorption units^{-1} was obtained and corresponding SO_2 uptake coefficients in the TiO_2+ (CO_2) + SO_2 system were thus estimated.

For SO_2 uptake in the TiO_2-($CaCO_3$) + SO_2 system, we estimated SO_2 uptake coefficients using three conversion curves established for various types of dust particles. For this sake, we mixed known proportion of K_2SO_4 and selected dust particles, and thus obtained relationship curves between the integrated absorbance of DRIFTS sulfate bands (1300-1100 cm^{-1}) and corresponding theoretical sulfate ions through linear fitting (Fig. S4).

Supplement Text 6

Gas sources and configuration setup. All gases used for experiments were purchased from Shanghai TOMOE gases CO., LTD. SO_2 (a mixture of 2.46×10^{15} molecule cm^{-3} SO_2 and balance gas N_2), CO_2 (a mixture of 2.46×10^{17} molecule cm^{-3} and balance gas N_2 or pure CO_2), and air with ultra-high purity of 99.999% were used as received. To precisely control the gas flow and concentrations, mass flow controllers (Beijing Sevenstar Electronics Co., Ltd.) were employed to adjust SO_2 or CO_2+SO_2 flows to the required concentration. With regard to the relative humidity (RH) adjustment, one pure dry air (21% O_2 and 79 % N_2) flow was humidified in a bubbler loaded with ultrapure water (electrical resistivity=18.2 MΩ). Together with rest gas flow equipped with MCFs, mixed gas with desired RH could be achieved. However, it should be noted that gas flow should be mixed for at least 1 h to reach a stable status before it is allowed to be introduced into DRIFTS or a home-made quartz chamber (d= 5.5 cm, H=1.2 cm, and actual volume= 20 cm^3).

Supplement Text 7

Mineral dust pretreatment and characterizations. Degussa TiO_2 was used as reference dust particles in all tests. A pretreatment process was performed to remove the organic impurities and inorganic impurities such as bicarbonate and carbonate at TiO_2 particle surfaces using a thermal heating method with a moderate heating rate of 2 ℃ min^{-1} at 400 ℃ for five hours in a tube furnace with the protection gas flow (dry air, 100 mL min^{-1}). Similar to the procedures applied for the particles in TiO_2+CO_2 +SO_2 system, particles TiO_2 and $CaCO_3$ (Aladdin industrial Co., LTD) in the TiO_2-($CaCO_3$) + SO_2 system were separately calcined at 500 ℃ for 3 h with protection gas flow (dry air, 100 mL min^{-1}). Similarly, SiO_2 and Al_2O_3 (Aladdin industrial Co., LTD) went through heat pretreatment described above (500 ℃ for 3 h). Mixtures of SiO_2, Al_2O_3, $CaCO_3$ and TiO_2 were prepared by manually grinding in the agate mortar. The crystalline phase of TiO_2 dust powder was analyzed by diffractometer with a Cu-Ka source. In addition, Brunauer-Emmet-Teller (BET) adsorption isotherm measurements were as well conducted using a Microm-eritics Asap 2000 surface area analyzer.

Supplement Text 8

***In situ* DRIFTS measurements.** To investigate the surface species during the heterogeneous reactions of SO_2 on mineral dust particles TiO_2, in situ diffuse reflectance Fourier transformed infrared spectroscopy *(in situ* DRIFTS, IRTracer-100, Shimadzu Instrument Corporation) was applied. Those FTIR spectra ranging from 4500 to 700 cm^{-1} were collected by using high-sensitivity mercury cadmium telluride (MCT) detector with a resolution of 4 cm^{-1} for 100 scans and recorded by diffuse reflectance accessory. Thermocouple wires attached to the ceramic sample holder and a temperature controller were used, allowing resistive heating from simulated solar light (250 W xenon lamp, Beijing CEAULIGHT Co.Ltd., China) during the reaction. Moreover, a cooling circulation device was applied considering the temperature fluctuation of samples due to the long-term exposure to the light source. All measurements were carried out at 298 K. Prior to reaction gas entering into the cell, further pretreatment was performed by sending dry airflow to the DRIFTS chamber under light irradiation for 1 h to remove the contamination residual on particle samples.

Supplement Text 9

IC measurements. Sulfate ions formed on dust particles during the reaction were investigated by IC using a Metrohm 883 Basic IC system equipped with a Metrosep A supply 5-250/4.0 analytical column and a conductivity detector. Sample particles after reaction were extracted by an oscillator. The leaching solution (3 % formaldehyde solution applied for TiO_2+ (CO_2) + SO_2 and 2 % isopropanol that applied for TiO_2-$CaCO_3$ +SO_2 were prepared using ultrapure water of 18.2 Ω). These solutions served as a preservative to avoid SO_2 (ad) oxidation during the extraction through a 0.22 μm PTFE membrane filter, followed by IC measurement. In this work, we employed a scrubber system with an eluent of 3.2 mM Na_2CO_3/1.0 mM $NaHCO_3$ for anion measurement at a flow rate of 0.7 mL min^{-1}.

Supplement Text 10

Raman spectra. In this study, an XploRA confocal spectrometer (Jobin Yvon, Horiba Gr, France) was applied for investigating dust particles after reaction. The Raman scattering was excited by an external-cavity diode (532 nm) and coupled with a 50 × Olympus microscope objective (Olympus, 0.50 Numerical Aperture). Raman signals were acquired by a charge-coupled device (CCD) camera operating at 220 K with 1200 lines per mm diffraction grating. Samples after reaction were monitored at the range of 100-2000 cm^{-1} with twice repeated scans and 5 s exposure time per spectrum to give an overall view of mineral dust particles, carbonate, and formed sulfate species. A narrowing scanning from wavenumber 910 to 1050 cm^{-1}, with 40 s exposure time and 15 times repeated scans, was conducted to investigate sulfate species produced on dust particle surfaces.

Supplement Text 11

ESR measurements. Electron spin resonance (ESR) spectrometry was performed on a JES-FA200 Spectrometer and formed radicals using DMPO spin trap were recorded at room temperature for all measurements. The g factor in each data was calibrated using manganese standards. ESR spectrums were recorded after irradiation with a 500 W high-pressure mercury lamp (USH-500SC) for 2 min. The computer simulations of ESR spectrums were further conducted with the software Isotropic Radicals (Hagen, 2009) to identify active intermediates during the reaction course. For details, computer simulation of the four-line DMPO/ ·OH and six-line DMPO/$SO_3^{\cdot-}$ radical adduct were obtained by setting splitting constant of $a^N = a_\beta^H$; = 15.2 G, and a^N=14.7 G and a_β^H=16.05 G, respectively. Those employed constants compare favorably with the prior literature (Mottley and Mason, 1988).

Supplement Text 12

NTAS Measurements. We utilized a nanosecond transient absorption spectroscopy (NTAS), designed and made by Dalian Institute of Chemical Physics, to investigate the possible heterogeneous reaction channels of sulfate formation on dust particles in the presence and absence of carbonate ions. About 35 mJ of the Nd: YAG laser source (355 nm, laser pulse 9 ns) entered into suprasil self-masking cuvettes (1 cm optical path and actual volume= 4 mL). All transient absorption spectra averaged by 10 times parallel results were obtained at room temperature. In addition, a monochromator and a photomultiplier tube with a detection wavelength range from 200 to 800 nm enable us to monitor the major active intermediates in the mineral dust suspension system. To visualize the signal of carbonate radical, we here applied single exponential decay curves (Eq. **S6,** the left side of the forward slash) to fit the signal of $CO_3^{\cdot-}$ evolved from TiO_2 suspension containing carbonate ions. The consumption process of carbonate radicals in chain reactions is described by a single exponential growth curve (Eq. **S6,** the right side of the forward slash).

$$y=a+be^{-\frac{x}{\tau}}/y=A+Be^{\frac{x}{\tau}} \qquad [\mathbf{S6}]$$

where τ is the lifetime of carbonate radicals in each system. Constant functions were employed to fit the samples without NTA signals.

Supplement Text 13

Theoretical studies of two reaction routes for producing carbonate radicals. In the present system, one of the viable mechanisms for the formation of $CO_3^{\cdot-}$ is hydrogen atom transfer (HAT) reaction (Eq. **S7**) through $\cdot OH$ with HCO_3^-. Such optimized structures involved in the HAT process as a reactant (React), transition state for the reaction step (TS), and the resulting product (Prod) were displayed in Fig. S11A. In HAT reaction, HCO_3^- transfers a H atom to O atom in $\cdot OH$, leading to the formation of H_2O and $CO_3^{\cdot-}$. The corresponding calculated activation free energy barrier $\Delta G^{\neq}{}_{HAT}$ was 9.02 kcal mol^{-1}, which is low enough for the HAT reaction of $\cdot OH$ and HCO_3^- to occur rapidly. The rate constant $k_{HAT\text{-}1}$ predicted for the HAT reaction was 4.04 ×10^6 $M^{-1}s^{-1}$.

$$\cdot OH+HCO_3^- \xrightarrow{k_{HAT\text{-}1}} CO_3^{\cdot-}+H_2O \qquad [\mathbf{S7}]$$

In addition, the formation of $CO_3^{\cdot-}$ could be also through the SET reaction (Eq. **S8**) of $\cdot OH$ with CO_3^{2-}. As shown in Fig. S11B, O atom in CO_3^{2-} transfers an electron to O atom in $\cdot OH$ to form $CO_3^{\cdot-}$ and OH^-. This SET reaction is thermodynamically favorable, with the difference of Gibbs free energy between reactant and product $\Delta G^0{}_{SET}$ lying at -9.74 kcal mol^{-1}. The corresponding calculated activation free energy barrier $\Delta G^0{}_{SET}$ is 0.02 kcal mol^{-1}, which is low enough for this thermal process to be faster than that controlled by the diffusion. Thus, the SET process for ·OH and $CO_3^{2-}$is diffusion-controlled. The rate constant $k_{SET\text{-}2}$ predicted for SET process between ·OH and CO_3^{2-} was 7.65×10^9 $M^{-1}s^{-1}$.

$$\cdot OH+CO_3^{2-}\xrightarrow{k_{SET\text{-}2}}CO_3^{\cdot -}+OH^{-} \quad \textbf{[S8]}$$

Supplement Text 14

Methodology for DFT calculations. All electronic calculations were performed using Gaussian 09 program (M. J. Frisch, 2009). In recent years, numerous benchmarks concerning the performance of different Density Functional Theory (DFT) methods have proved that M06-2X functional is a reasonable choice for computing thermochemistry and barrier of atmospheric relevant systems (Zhao and Truhlar, 2008;Elm et al., 2012;Mardirossian and Head-Gordon, 2016;Pereira et al., 2017). Hence, geometry optimization of all the investigated species, including reactants, products, and transition states and frequency calculation have been performed using the M062X functional coupled with the 6-311++G(3df, 3pd) basis set. Single point energy was calculated at CCSD(T)-F12/cc-PVDZ-F12 level of theory by ORCA 4.10 program using the geometry optimized at M06-2X/6-311++G(3df, 3pd) level (Neese, 2012;Peterson et al., 2008;Yousaf and Peterson, 2008;Lane and Kjaergaard, 2009;Knizia et al., 2009). In order to mimic the implicit solvent environment (Marenich et al., 2009), the solvation effect was introduced through the continuum solvation model based on solute electron density (SMD). The free energy in the solution was obtained using Eq. **S9**:

$$G^0 \quad =E_0^{\mathrm{CCSD(T)\text{-}F12}}+G_{\mathrm{corr}}^{\mathrm{M06\text{-}2X}}+\Delta G_{\mathrm{SMD}}^{\mathrm{M06\text{-}2X}}+\Delta G_{\mathrm{1atm\rightarrow 1M}} \quad \textbf{[S9]}$$

$E_0^{\mathrm{CCSD(T)\text{-}F12}}$ is the electronic energy obtained at the CCSD(T)-F12/cc-PVDZ-F12 level, $G_{\mathrm{corr}}^{\mathrm{M06\text{-}2X}}$is the thermal correction to Gibbs free energy at the M06-2X/6-311++G(3df, 3pd) level under standard conditions (T=298K, P=1 atm), $\boldsymbol{\Delta}G_{\mathrm{SMD}}^{\mathrm{M06\text{-}2X}}$is the solvation free energy obtained from single point calculation at the M06-2X/6-311++G (3df, 3pd) level and $\boldsymbol{\Delta}G_{\mathrm{1atm\rightarrow 1M}}$ is an additional term for converting the standard pressure of 1 atm in the gas phase to the standard concentration of 1 mol L^{-1} in solution (1.89 kcal mol^{-1}) (Marenich et al., 2009).

In the present system, one of the viable mechanisms to describe reaction process is the hydrogen atom transfer (HAT) reaction. In this kind of reaction, transition states are necessary for calculating the activation free energy barrier term in HAT reaction. k_{act}, the thermal rate constant determined by activation free energy barrier, was calculated using the conventional Transition State Theory (TST)(Eyring, 1935;Evans and Polanyi, 1935;Truhlar et al., 1983) as implemented in 1 M standard state (Eq. **S10**):

$$k_{act}=l\kappa(T)\frac{k_BT}{h}\exp\left(\frac{-\Delta G^{\neq}}{RT}\right) \quad \textbf{[S10]}$$

Where l is the reaction path degeneracy accounting for the number of equivalent reaction paths. $\kappa(T)$, a temperature-dependent factor, corresponds to quantum mechanical tunneling and is approximated by Eq. **S11** according to Wigner (Elm et al., 2013;Wigner, 1932) for the HAT reaction; k_{B} is Boltzmann's constant, h is Plank's constant, and R is gas constant.

$$\kappa(T)=1+\frac{1}{24}\left(\frac{h\nu^{\mu}}{k_BT}\right)^2 \quad \textbf{[S11]}$$

However, for a single electron transfer (SET) reaction, transition state cannot be located using electronic structure methods, as it is not possible to describe the mechanistic pathway of electron motion. To estimate the reaction activation free energy barrier ($\Delta G^{\neq}$term), in such cases, the Marcus theory was used (Marcus, 1997a, b). Within this transition-state formalism, the SET reaction activation free energy barrier ($\Delta G^{\neq}{}_{\mathrm{SET}}$) is defined in terms of the difference of the Gibbs free energy between reactants and the products ($\Delta G^{0}{}_{\mathrm{SET}}$) in SET reaction and the nuclear reorganization energy (λ) as follows (Eq. **S12**):

$$\Delta G^{\neq}{}_{\mathrm{SET}}=\frac{(\lambda+\Delta G^{0}{}_{\mathrm{SET}})^2}{4\lambda} \quad \textbf{[S12]}$$

While for λ, a very simple approximation was used as Eq. **S13**:

$$\lambda=\Delta E\text{-}\Delta G^{0}{}_{\mathrm{SET}} \quad \textbf{[S13]}$$

Where $\boldsymbol{\Delta}E$ is the non-adiabatic energy difference between reactants and vertical products.

It is expected that the tunneling effect would not be large for the reactions with low barriers (Iuga et al., 2015;Luo et al., 2017). Therefore, the tunneling effect was neglected in this SET reaction for its low barriers which will be discussed in detail in the R&D Section. In addition, diffusion should be considered especially for the low barrier SET reaction with k_{act} approximated to the diffusion limit (Luo et al., 2017). Thus, the Collins-Kimball theory(Kimball, 1949) was used to calculate the total rate constant k_{SET} or k_{HAT} that can be expressed as Eq. **S14**:

$$k_{\mathrm{SET}}(k_{\mathrm{HAT}}) = \frac{k_D k_{act}}{k_D + k_{act}} \quad \textbf{[S14]}$$

Where k_D is the steady-state Smoluchowski rate constant (Smoluchowski, 1917) for an irreversible bi-molecular diffusion-controlled reaction. Smoluchowski (Raymond, 2000) developed an empirical equation to calculate diffusion-controlled reaction rate constant k_D in an aqueous solution (Eq. **S15**):

$$k_D = \frac{2N_A k_B T(r_1+r_2)^2}{3\eta r_1 r_2} \quad \textbf{[S15]}$$

Where N_A is the Avogadro constant, k_B is Boltzmann constant, T is temperature, η is the viscosity of water, and r_1, r_2 are the radius of the bi-molecular reactants.

Supplement Text 15

The procedures for oxygen isotope experiments: Oxygen isotope experiments were divided into two parts: 1. preparation of $C^{18}O_2/N_2$ (2.46×10^{17} molecule cm^{-3}) through $C^{16}O_2$ exchanging with $H_2{}^{18}O$, 2. monitoring formed species using *in situ* DRIFTS. In the first step, a chamber was washed with ultrapure water (electrical resistivity= 18.2 MΩ), followed by drying the chamber using dry ultrapure N_2 gas flow (300 mL min^{-1}, 40 min). Afterward, we introduced $H_2{}^{16(18)}O$ into the chamber with a pipette and operated this process in the glove box with N_2 atmosphere, where contents of H_2O were rigorously controlled below 2.46×10^{13} molecule cm^{-3} to prevent the undesired exchange of ^{18}O with ^{16}O in the atmosphere. Followed by this step, we extracted the gas from the chamber and added it with CO_2 for O exchange (70 min). For these two sets of DRIFTS studies, TiO_2 particles went through in situ heat pretreatments in the sample holder with an airflow (150 mL min^{-1}) at 500℃ for 0.5 h. Subsequently, TiO_2 particles were cooled down to room temperature using a cooling device attached to the DRIFTS for 35 min. Then, the chamber was sealed with gas-tight sample pads and we evacuated the chamber and introduced $C^{16(18)}O_2/N_2$. After adsorption of CO_2/N_2 for 20 min, TiO_2 was exposed to 6.14×10^{15} molecule cm^{-3} of SO_2/N_2+O_2 (RH= 30 %) for 60 min and we monitored the sulfate formation under irradiation (light intensity (I) = 30 mW cm^{-2}) for each set of experiment.

Supplement Text 16

Sampling. Our sampling for atmospheric particle matter was launched on the roof of the environmental science and engineering department, Fudan University (Jiangwan Campus, 31.340661°N, 121.506747°E, 16 km away from the city downtown. Observations for water-soluble ionic components of particle matter were performed using an 8-stage non-viable-cascade-impactor type sampler (TISCH TE Inc., USA), size gradient of which are in the sequence of < 0.43, 0.43- 0.65, 0.65-1.1, 1.1- 2.1, 2.1- 3.3, 3.3- 4.7, 4.7- 5.8 5.8- 9.0 and 9.0~ μm. These sizes represent the effective cutoff diameter at each level for unit density spherical particles. In our sampling, the estimations for (bi)carbonate ions in atmospheric particulate matter mainly focus on the initial four stages (3.3~ μm). Atmospheric airflow from the head was maintained at the constant 28.3 L min^{-1} to meet the operation required for the Anderson-type sampler configuration. Quartz filters (81 mm in diameter, Whatman, GE Healthcare, UK) were employed for sampling operations, and membranes were pretreated with ultrapure water (electrical resistivity= 18.2 MΩ) no less than three times (kept in the ultrasonic cleaning tank for 40 min and then rinsed with ultrapure water for twice) before being sent into the infrared drying oven, followed by packing them in aluminum foils prior to field sampling. We carried out this procedure to eliminate the water-soluble background ions as much as possible and to ensure the balance calculation for (bi)carbonate ions. Additionally, blank membranes following the same aforementioned pretreatments were applied for measuring the background concentrations for ions. We separated our daily samplings into two periods, 11 hours for each, to give an insight into the influence of potential photo-induced reactions on secondary sulfate formation in the atmosphere.

Supplement Text 17

Chemical analyses. Water-soluble ions in the atmospheric particulate matter were measured using a Metrohm 883 Basic IC system, which is equipped with a Metrosep A Supply A-250/4.0 anion analytical column or a C-150/4.0 cation analytical column and a conductivity detector; eluent: 3.2 mM Na_2CO_3/1.0 mM $NaHCO_3$ for anion measurements at a flow rate of 0.7 mL min^{-1}; 1.7 mmol L^{-1} HNO_3 for cation measurements at a flow rate of 0.9 mL min^{-1}; inject volume: 20 uL. A series of Li^+, NH_4^+, Ca^{2+}, Mg^{2+}, Na^+, K^+, F^-, CH_3COO^-, $COOH^-$, Cl^-, NO_2^-, NO_3^-, PO_4^{3-}, SO_4^{2-}, and $C_2O_4^{2-}$ ions were analyzed. Each collected filter membrane was cut and placed into a 50 mL PET vial, followed by ultrasonically extracting for 40 min with 20 mL ultrapure water (R ≥ 18.0 MΩ). For each sample, we applied two PTFE filter chips to remove insoluble particulate matter before being sent into IC. Obtained ion concentration results were further transformed to the data in the unit of μg m^{-3} on the basis of Eq. **S16**:

$$\rho=\frac{(\rho_1-\rho_0)\times V\times N\times D}{V_{nd}}$$

[S16]

where ρ represents the ions concentration (μg m^{-3}), ρ_1 is the measured ions concentration of membrane after sampling (mg L^{-1}), ρ_0 is the measured ions concentration of membrane before sampling (mg L^{-1}), V is the volume of extracting solution for sample (L), and N refers to divisions for membrane, D to the dilution coefficient, and V_{nd} to the total sampling volume.

Supplement Text 18

(Bi)carbonate estimation. Two assumptions were made to simplify the estimation for bi(carbonate) ion concentrations within the system: a. dominating cation ions in each system are H^+, Li^+, Na^+, NH_4^+, K^+, $Mg^{2+}$and Ca^{2+} whereas those transition and heavy metal ions were out of consideration given their limited contents of dissolve cations in the atmospheric particulate matter; b. three typical organic acid ions (CH_3COO^-, $COOH^-$ and $C_2O_4^{2-}$, major soluble organic acid ions in the atmosphere) were taken into accounts for ionization balance and the rest of the charge gap in each system were assumed to originate from (bi)carbonate ions. Then we established balance equations (Eqs. **S17-20**) for each sample on the basis of charge conservation and ionization equilibrium constant of carbonic acid (K_1= 4.47 ×10^{-7} and K_2= 4.69 ×10^{-11}at 273 K).

$$[H^+]+ [Li^+]+ [Na^+]+ [NH_4^+]+ [K^+]+ 2[Mg^{2+}]+ 2[Ca^{2+}]=[OH^-]+ [F^-]+ [CH_3COO^-]+[COOH^-]+ [NO_2^-] +[Cl^-]+ [NO_3^-]+$$

$$3[PO_4^{3-}]+ 2[SO_4^{2-}]+ 2[C_2O_4^{2-}]+ [HCO_3^-]+ 2[CO_3^{2-}]$$

[S17]

$$[HCO_3^-]= \frac{K_1[H_2CO_3]}{[H^+]}$$

[S18]

$$[CO_3^{2-}]= \frac{K_1K_2[H_2CO_3]}{[H^+]^2}$$

[S19]

It worth mentioning that [X] is referred to charge concentration for ions (Coulomb·M). Additionally, the temperature factor was also considered to correct equilibrium constant for (bi)carbonate ions using the following equation:

$$\mathrm{Ln}\frac{K_{x'}}{K_x}=-\frac{\Delta H}{R}(\frac{1}{T_{x'}}-\frac{1}{T_x})$$

[S20]

where ΔH is the temperature variation (K), R the ideal gas constant (8.31451 J mol^{-1} K^{-1}), and T the temperature (K) during pH measurements. We then solved those equations to obtain a series of $[HCO_3^-]$, which were finally corrected by subtracting blank values.

Table S1. Chemical compositions of dust simulants.

	SiO_2 (wt. %) [†]	Al_2O_3 (wt. %) [†]	$CaCO_3$ (wt. %) [*,†]	TiO_2 (wt. %) [†]
SiO_2-Al_2O_3	89.46	10.54	-	-
SiO_2-Al_2O_3-$CaCO_3$	82.47	9.72	7.81	-
SiO_2-Al_2O_3-TiO_2	88.42	10.42	-	1.15
SiO_2-Al_2O_3-TiO_2 -$CaCO_3$	81.59	9.62	7.73	1.06

*In the present study, $CaCO_3$ was taken as representative of alkaline-earth metal oxide in our proxies for the authentic dust.

[†] The mass ratio of 4 components (when doped) in the authentic particles were controlled in the ratio of SiO_2:Al_2O_3:$CaCO_3$: TiO_2= 81.59: 9.62:7.73:1.06. For instance, the ratio of SiO_2 to Al_2O_3 is 81.59: 9.62 in the SiO_2-Al_2O_3 simulant, and 81.59: 9.62:7.73 in the SiO_2-Al_2O_3-$CaCO_3$ mixture.

Table S2. Chemical Compositions of the ATD Dust and Standard Clays.

Minerals	ATD (%)*	IMt-2 (%)*	KGa-2 (%)*
SiO_2	78.11	59.57	56.93
Al_2O_3	7.19	19.47	37.49
Fe_2O_3	2.57	7.95	1.81
FeO	n.d. †	0.05	0.15
MgO	1.22	2.42	0.03
CaO	3.03	0.37	0.01
Na_2O	1.39	0.08	n.d. †
K_2O	2.06	8.72	0.06
TiO_2	0.46	0.99	3.43
P_2O_5	0.10	0.07	0.05
MnO	0.04	0.03	n.d.†
S	n.d. †	0.03	0.02
Total	99.21	99.75	99.98
Total A.E. ‡	7.70	11.59	0.10

*Chemical compositions of the dust and clays were determined by XRF results.

†n.d. refers to not detected.

‡A.E. refers to alkaline earth metal oxide.

Table S3. Estimation for Sulfate Formation Rate and Uptake Coefficient of SO_2.

	Carbonate Fraction (wt. %) / CO_2 Concentration ($\times 10^{15}$ molecule cm^{-3})	Sulfate Formation Rate ($\times 10^{12}$ ion s^{-1})	Uptake Coefficient ($\times 10^{-5}$)
TiO_2-$CaCO_3$+SO_2	0	2.55 ± 0.04	1.17 ± 0.02 *
	50	45.76 ± 0.56	20.89 ± 0.24
	100	2.68 ± 0.32	1.23 ± 0.15
TiO_2+CO_2+SO_2	0	2.37 ± 0.16	2.23 ± 0.02 *
	4.91	3.03 ± 0.27	2.80 ± 0.25
	9.83	3.59 ± 0.49	3.38 ± 0.05

* It is notable that difference would take place with regard to the uptake coefficients of pristine TiO_2 in the TiO_2-($CaCO_3$)+SO_2 and TiO_2+(CO_2)+SO_2 systems. This is mainly due to the different reaction conditions and varied approaches for uptake estimations in these two systems.

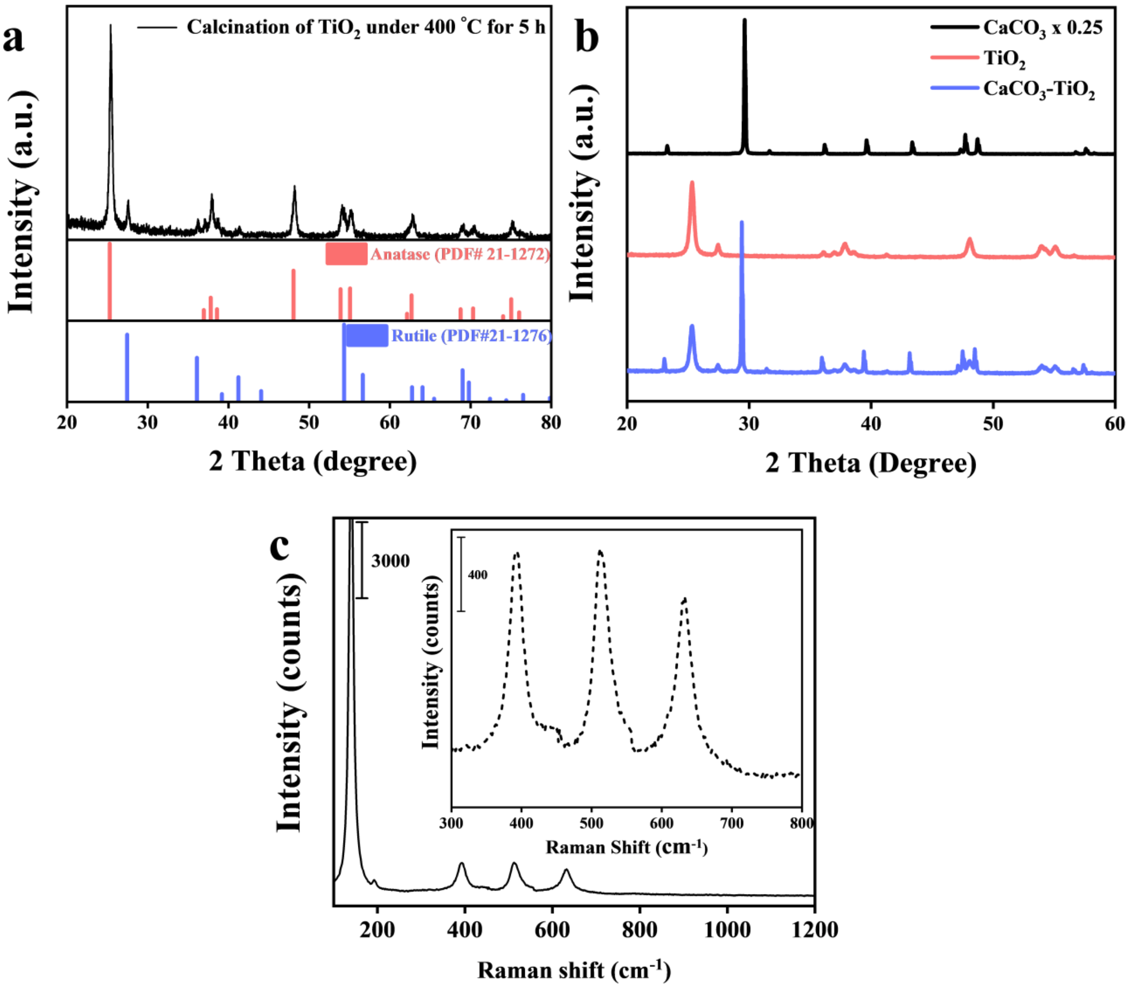

Fig. S1. Characterizations of mineral dust particles. XRD patterns of TiO_2 (**a**) and $CaCO_3$ (**b**) particles, respectively. (**c**) Raman spectra of TiO_2 particle. Standard PDF cards for anatase and rutile phases of TiO_2 were compared as a reference.

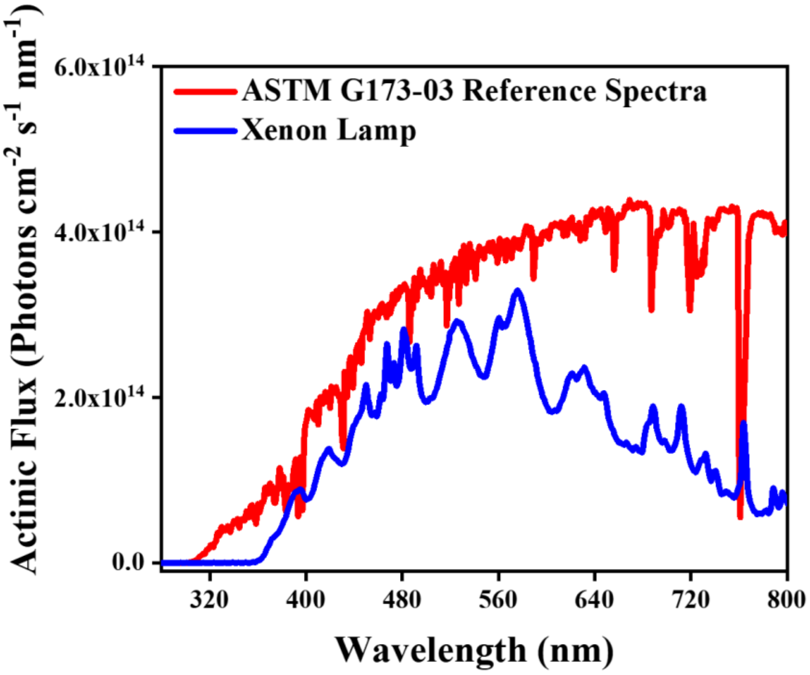

Fig. S2. The actinic flux of solar irradiance spectra ASTM G173-03 and a xenon lamp. ASTM G173-03 refers to the "Standard Tables for Reference Solar Spectral Irradiances: Direct Normal and Hemispherical on 37deg; Tilted Surface", which served as a reference spectra for comparison.

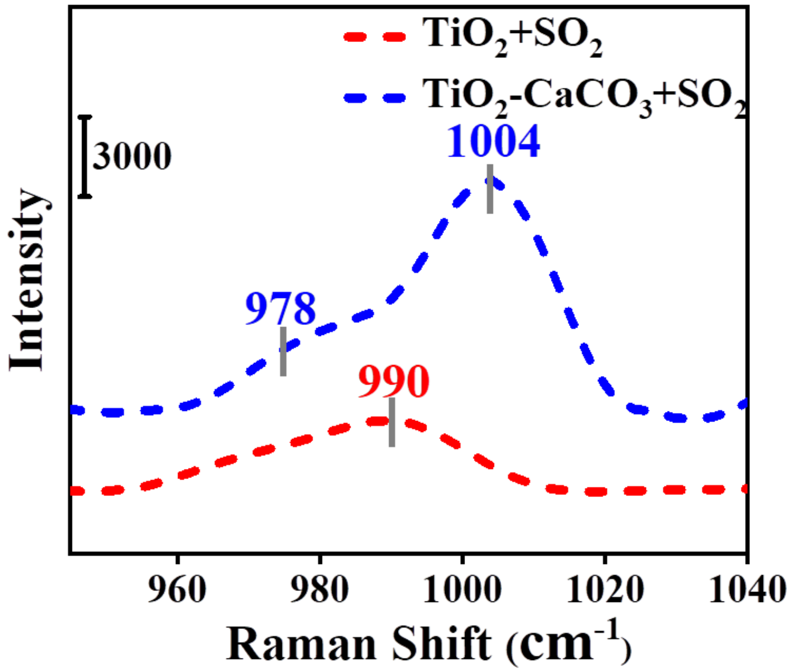

Fig. S3. Raman spectra of mineral dust particles after reaction. Those particles for Raman analysis were referred to 50 wt.% TiO_2-50 wt.% $CaCO_3$ and exposed to 2.21×10^{14} molecule cm^{-3} SO_2/N_2+O_2 under illumination in the home-made reaction chamber.

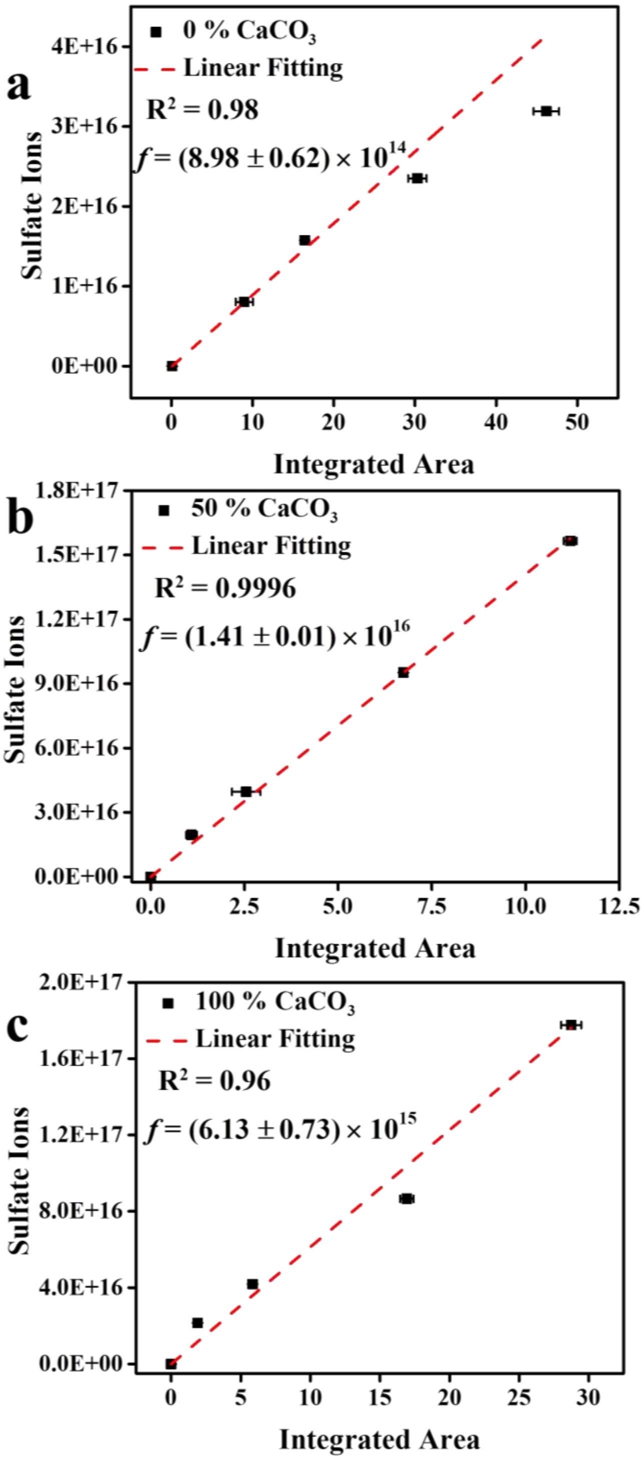

Fig. S4. Calculation of the conversion factor for each type of particle of interest. The infrared absorption calibration curves were obtained using known proportions of K_2SO_4 and dust particles (**a**) TiO_2, (**b**) 50 wt.% TiO_2-50 wt.% $CaCO_3$ and (**c**) $CaCO_3$, respectively. Uncertainties on conversion factors represent the standard deviation of the slopes obtained from the linear regression analysis.

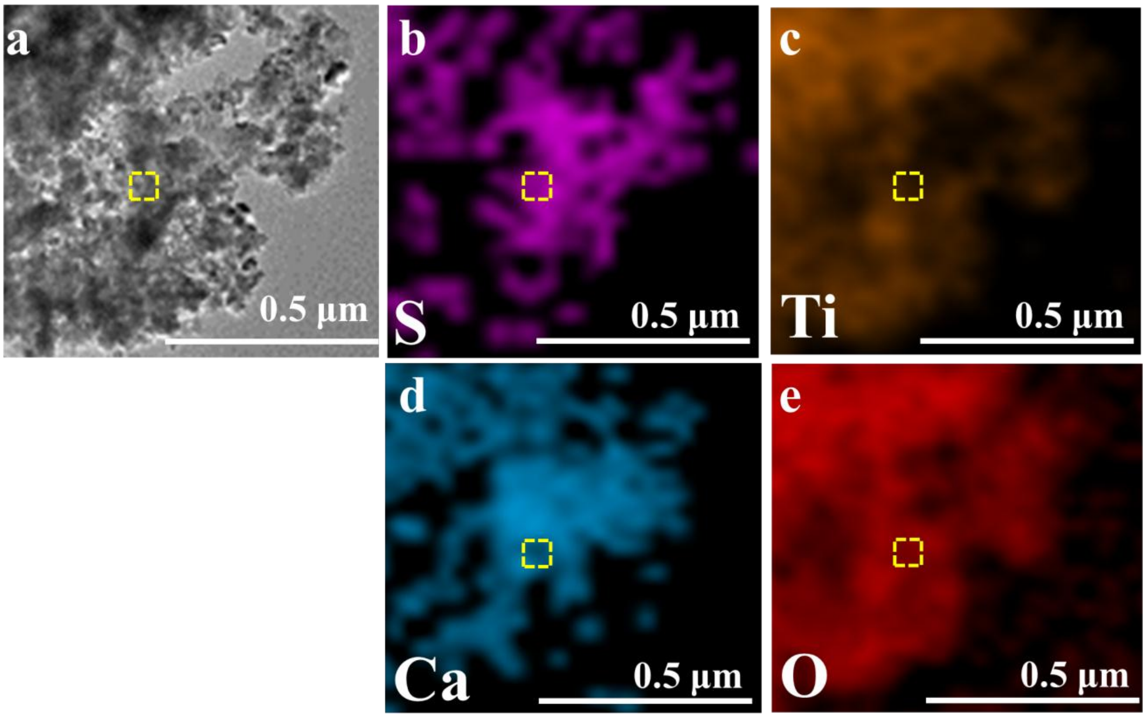

Fig. S5. The HRTEM image: (**a**) and element mappings (**b-e**) for dust particles after reaction. 50 wt. % $CaCO_3$-50 wt. % TiO_2 particles after being exposed to the SO_2/N_2+O_2 gas flow for 60 min. Reaction condition: $[SO_2] = 4.4\times10^{14}$ molecule cm^{-3}, RH= 30 % and Irradiation intensity = 30 mW cm^{-2}.

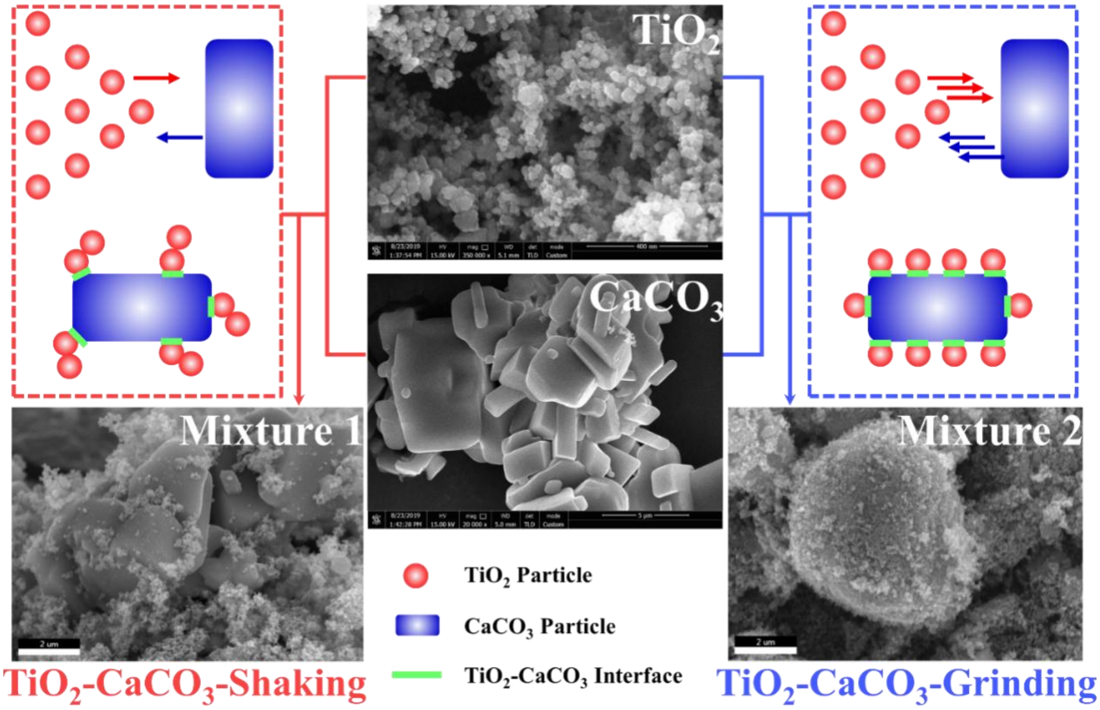

Fig. S6. Scanning electron microscope (SEM) of concerned particles. Noting that the mixture 1 and 2 refer to the particles composed of 50 % mass fraction of TiO_2 and 50 % mass fraction of $CaCO_3$ prepared through manually-shaking method and manually-grinding method, respectively.

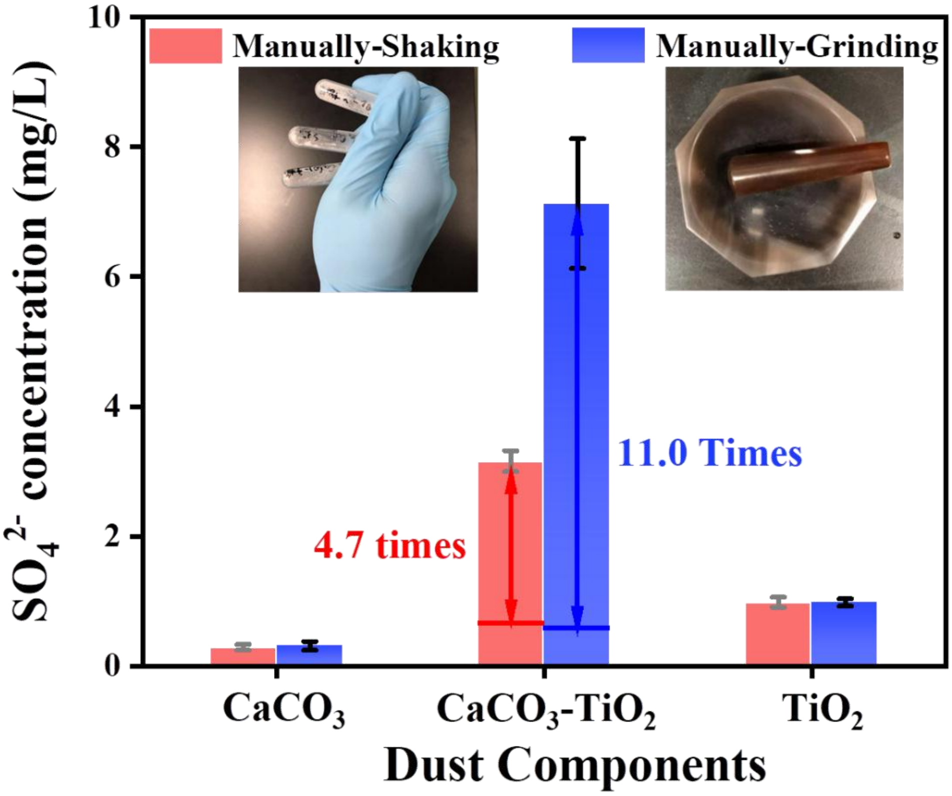

Fig. S7. The heterogeneous reaction of SO_2 on mineral dust surfaces in two $CaCO_3$-TiO_2 systems. Sulfate concentration measured by IC on mineral dust surfaces after exposure to gaseous SO_2 under irradiation. Reaction condition: SO_2 concentration = 2.21×10^{14} molecule cm^{-3}, RH= 30 % and Light intensity (I) = 30 mW cm^{-2}. Theoretical sulfate concentration of TiO_2-$CaCO_3$ mixtures in each system was obtained from a simple linear superposition of the IC results of individual components and enhancement factors for sulfate ions in two systems could be thus estimated. Prior to each experiment, a dry airflow of 80 mL min^{-1} (15 min) was applied.

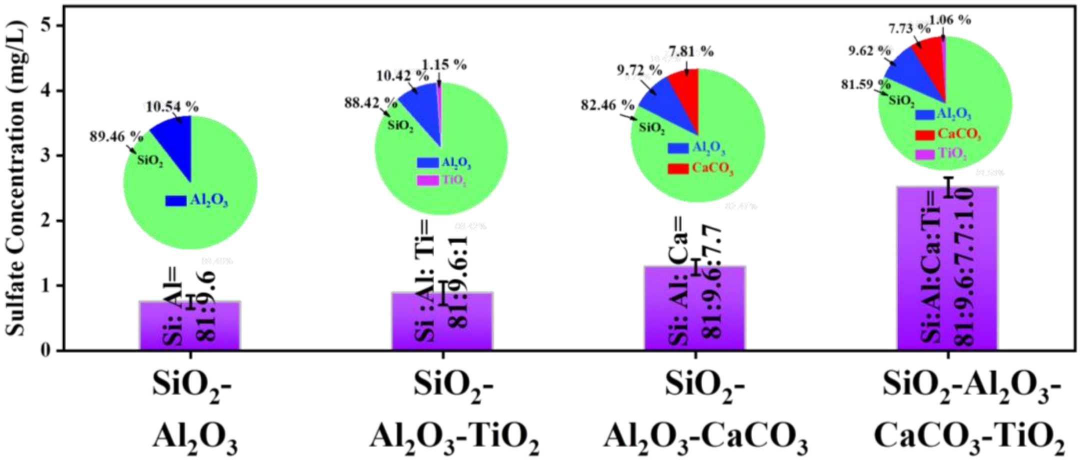

Fig. S8. Sulfate concentration quantified by IC. Sulfate concentration was measured by IC on mineral dust simulants after exposure to gaseous SO_2 (2.46×10^{14} molecule cm^{-3}) under irradiation. Noting that SiO_2: Al_2O_3: $CaCO_3$: TiO_2 refers to the mass fraction ratios of the components in simulants. Experiments were all conducted at RH of 30 % and Light intensity (*I*) of 30 mW cm^{-2}.

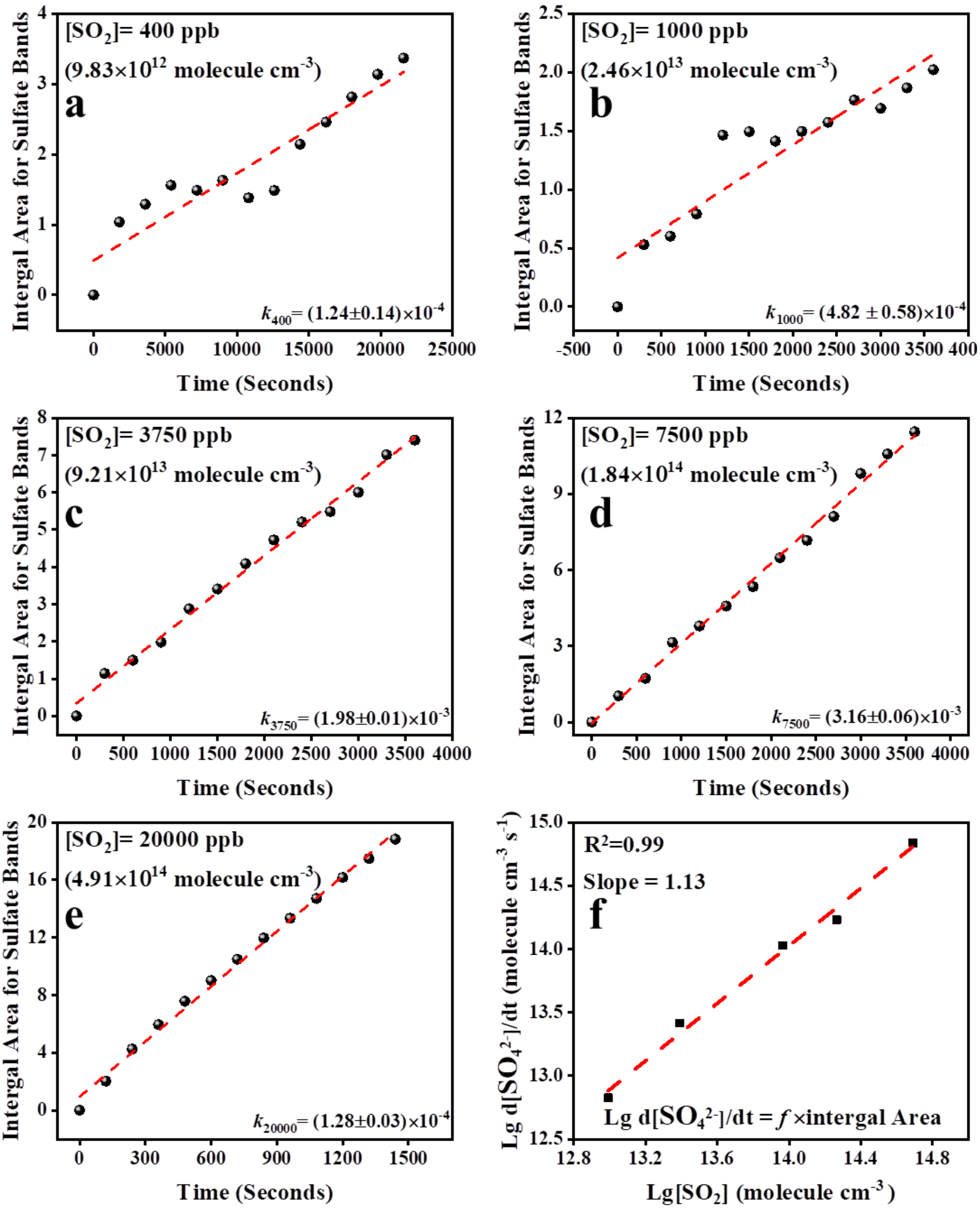

Fig. S9. Reaction order determination. (**a-e**) The sulfate formation rate on TiO_2 under varied SO_2 concentration (400- 20000 ppb) in the presence of CO_2 (400 ppm) with irradiation (30 mW cm^{-2}). (**f**) The lg-Lg curve of the sulfate production rate plotted against the exposed SO_2 molecules.

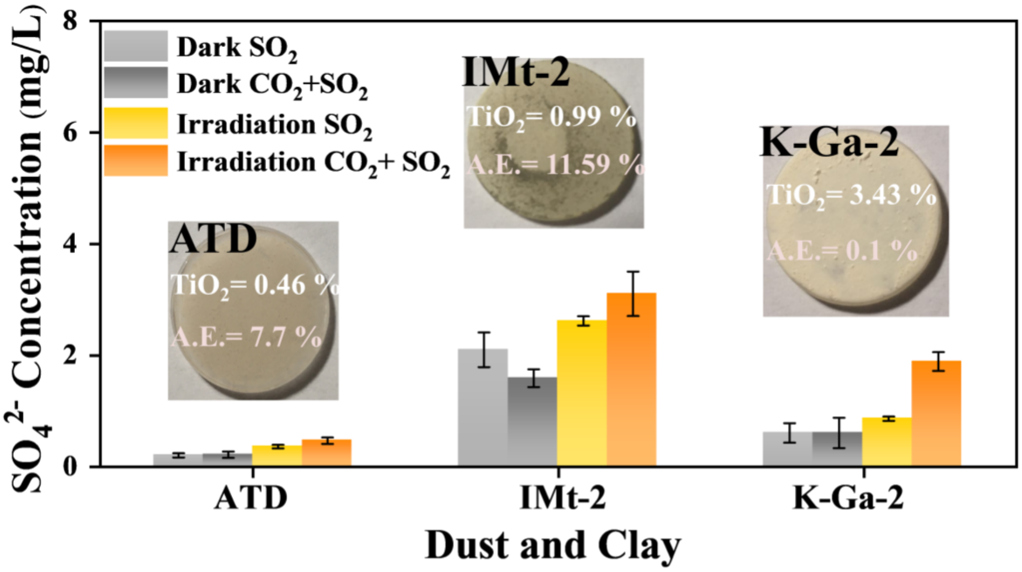

Fig. S10. Laboratory studies of sulfate production on authentic dust and clay membranes under the dark and irradiation (30 mW cm^{-2}) upon exposure to 4.91×10^{14} molecules cm^{-3} SO_2/N_2+O_2 and 2.46×10^{18} molecules cm^{-3} CO_2+ 4.91×10^{14} molecules cm^{-3} SO_2/N_2+O_2 at RH of 30 % (total flow rate = 100 mL min^{-1}).

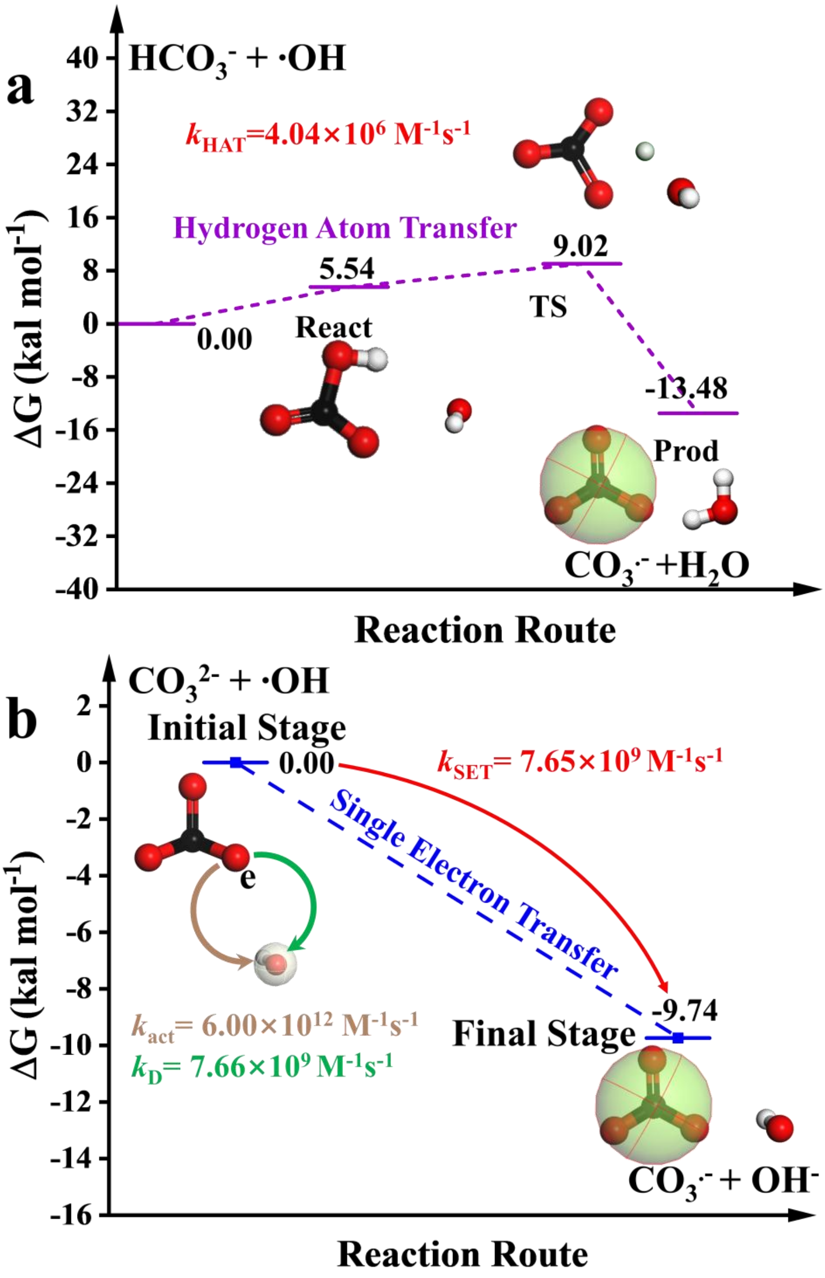

Fig. S11. DFT calculations of two reaction routes for producing carbonate radicals. (**a**) Reaction energy profiles (kcal mol^{-1}) of the HAT reaction through ·OH with HCO_3^- at the CCSD(T)-F12/cc-PVDZ-F12//M06-2X/6-311++G (3df, 3pd) level. The white, black, and red spheres represent H, C, and O atoms, respectively. (**b**) Reaction pathway of the hydroxyl radical (·OH) and CO_3^{2-} through the SET process at the CCSD(T)-F12/cc-PVDZ-F12//M06-2X/6-311++G (3df, 3pd) level, and ΔG^0_{SET} is the difference of Gibbs free energy between reactants and products.

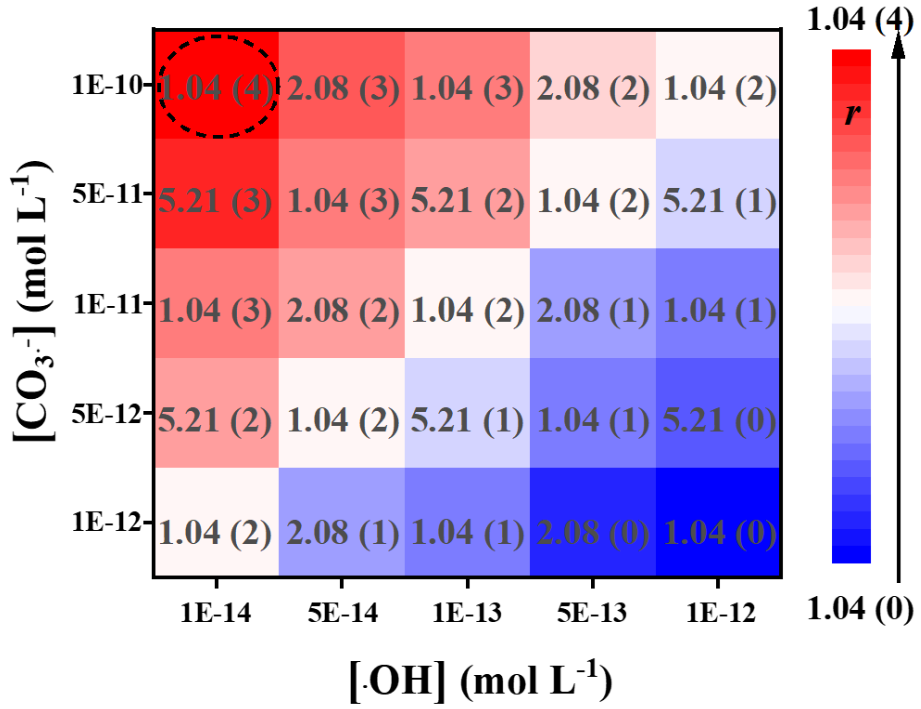

Fig. S12. The ratio of the two reaction rates *r* versus the concentration of $CO_3^{\cdot-}$ and ·OH. Numbers in parentheses referred to powers of ten.

Reference

Balachandran, U., and Eror, N. G.: Raman-Spectra Of Titanium-Dioxide, J. Solid State Chem., 42, 276-282, https://doi.org/10.1016/0022-4596(82)90006-8, 1982.

Elm, J., Bilde, M., and Mikkelsen, K. V.: Assessment of Density Functional Theory in Predicting Structures and Free Energies of Reaction of Atmospheric Prenucleation Clusters, J. Chem. Theory. Comput., 8, 2071-2077, https://doi.org/10.1021/ct300192p, 2012.

Elm, J., Jorgensen, S., Bilde, M., and Mikkelsen, K. V.: Ambient reaction kinetics of atmospheric oxygenated organics with the OH radical: a computational methodology study, Phys. Chem. Chem. Phys., 15, 9636-9645, https://doi.org/10.1039/c3cp50192b, 2013.

Evans, M. G., and Polanyi, M.: Some applications of the transition state method to the calculation of reaction velocities, especially in solution., T. Faraday Soc., 31, 0875-0893, https://doi.org/10.1039/Tf9353100875, 1935.

Eyring, H.: The activated complex in chemical reactions, J. Chem. Phys., 3, 107-115, https://doi.org/10.1063/1.1749604, 1935.

Franchin, A., Ehrhart, S., Leppa, J., Nieminen, T., Gagne, S., Schobesberger, S., Wimmer, D., Duplissy, J., Riccobono, F., Dunne, E. M., Rondo, L., Downard, A., Bianchi, F., Kupc, A., Tsagkogeorgas, G., Lehtipalo, K., Manninen, H. E., Almeida, J., Amorim, A., Wagner, P. E., Hansel, A., Kirkby, J., Kurten, A., Donahue, N. M., Makhmutov, V., Mathot, S., Metzger, A., Petaja, T., Schnitzhofer, R., Sipila, M., Stozhkov, Y., Tome, A., Kerminen, V. M., Carslaw, K., Curtius, J., Baltensperger, U., and Kulmala, M.: Experimental investigation of ion-ion recombination under atmospheric conditions, Atmos. Chem. Phys., 15, 7203-7216, https://doi.org/10.5194/acp-15-7203-2015, 2015.

Iuga, C., Campero, A., and Vivier-Bunge, A.: Antioxidant vs. prooxidant action of phenothiazine in a biological environment in the presence of hydroxyl and hydroperoxyl radicals: a quantum chemistry study, Rsc Adv., 5, 14678-14689, https://doi.org/10.1039/c4ra14918a, 2015.

Kimball, F. C. C. a. G. E.: DIFFUSION-CONTROLLED REACTION RATES, J. Colloid Interf. Sci., 4, 425-437, https://doi.org/10.1016/0095-8522(49)90023-9, 1949.

Knizia, G., Adler, T. B., and Werner, H. J.: Simplified CCSD(T)-F12 methods: Theory and benchmarks, J. Chem. Phys., 130, https://doi.org/10.1063/1.3054300, 2009.

Kong, L. D., Zhao, X., Sun, Z. Y., Yang, Y. W., Fu, H. B., Zhang, S. C., Cheng, T. T., Yang, X., Wang, L., and Chen, J. M.: The effects of nitrate on the heterogeneous uptake of sulfur dioxide on hematite, Atmos. Chem. Phys., 14, 9451-9467, https://doi.org/10.5194/acp-14-9451-2014, 2014.

Lane, J. R., and Kjaergaard, H. G.: Explicitly correlated intermolecular distances and interaction energies of hydrogen bonded complexes, J. Chem. Phys., 131, https://doi.org/10.1063/1.3159672, 2009.

Luo, S., Wei, Z. S., Dionysiou, D. D., Spinney, R., Hu, W. P., Chai, L. Y., Yang, Z. H., Ye, T. T., and Xiao, R. Y.: Mechanistic insight into reactivity of sulfate radical with aromatic contaminants through single-electron transfer pathway, Chem. Eng. J., 327, 1056-1065, https://doi.org/10.1016/j.cej.2017.06.179, 2017.

M. J. Frisch, G. W. T., H. B. Schlegel, G. E. Scuseria, M. A. Robb, J. R. Cheeseman, G. Scalmani, V. Barone, B. Mennucci, G. A. Petersson, H. Nakatsuji, M. Caricato, X. Li, H. P. Hratchian, A. F. Izmaylov, J. Bloino, G. Zheng, J. L. Sonnenberg, M. Hada, K. Ehara, M Toyota, R. Fukuda, J. Hasegawa, M. Ishida, T. Nakajima, Y. Honda, O. Kitao, H. Nakai, T. Vreven, J. A. Montgomery, J. E. Peralta, F. Ogliaro, M. Bearpark, J. J. Heyd, E. Brothers, K. N. Kudin, V. N. Staroverov, R. Kobayashi, J. Normand, K. Raghavachari, A. Rendell, J. C. Burant, S. S. Iyengar, J. Tomasi, M. Cossi, N. Rega, J. M. Millam, M. Klene, J. E. Knox, J. B. Cross, V. Bakken, C. Adamo, J. Jaramillo, R. Gomperts, R. E. Stratmann, O. Yazyev, A. J. Austin, R. Cammi, C. Pomelli, J. W. Ochterski, R. L. Martin, K. Morokuma, V. G. Zakrzewski, G. A. Voth, P. Salvador, J. J. Dannenberg, S. Dapprich, A. D. Daniels, O. Farkas, J. B. Foresman, J. V. Ortiz, J. Cioslowski and D. J. Fox: Gaussian 09, Revision A.1 ed., , Gaussian Inc., Wallingford CT, 2009.

Marcus, R. A.: J Electroanal Chem, 438, 251-259, 1997a.

Marcus, R. A.: Pure Appl. Chem., 69, 13-29, 1997b.

Mardirossian, N., and Head-Gordon, M.: How Accurate Are the Minnesota Density Functionals for Noncovalent Interactions, Isomerization Energies, Thermochemistry, and Barrier Heights Involving Molecules Composed of Main-Group Elements?, J. Chem. Theory. Comput., 12, 4303-4325, https://doi.org/10.1021/acs.jctc.6b00637, 2016.

Marenich, A. V., Cramer, C. J., and Truhlar, D. G.: Performance of SM6, SM8, and SMD on the SAMPL1 Test Set for the Prediction of Small-Molecule Solvation Free Energies, J. Phys. Chem. B, 113, 4538-4543, https://doi.org/10.1021/jp809094y, 2009.

Mottley, C., and Mason, R. P.: Sulfate Anion Free-Radical Formation by the Peroxidation Of (Bi)Sulfite And Its Reaction with Hydroxyl Radical Scavengers, Arch. Biochem. Biophys., 267, 681-689, https://doi.org/10.1016/0003-9861(88)90077-X, 1988.

Neese, F.: The ORCA program system Wires. Comput. Mol. Sci., 2, 73-78, https://doi.org/10.1002/wcms.81, 2012.

Pereira, A. T., Ribeiro, A. J. M., Fernandes, P. A., and Ramos, M. J.: Benchmarking of density functionals for the kinetics and thermodynamics of the hydrolysis of glycosidic bonds catalyzed by glycosidases, Int. J. Quantum. Chem., 117, https://doi.org/10.1002/qua.25409, 2017.

Peterson, K. A., Adler, T. B., and Werner, H. J.: Systematically convergent basis sets for explicitly correlated wavefunctions: The atoms H, He, B-Ne, and Al-Ar, J. Chem. Phys., 128, https://doi.org/10.1063/1.2831537, 2008.

Raymond, C.: Physical Chemistry for the Chemical and Biological Sciences, 3rd ed., University Science Books, Sausalito,CA, 2000.

Shang, J., Li, J., and Zhu, T.: Heterogeneous reaction of SO_2 on TiO_2 particles, Sci. China Chem., https://doi.org/10.1007/s11426-010-4160-3, 2010.

Smoluchowski, M. V.: Mathematical Theory of the kinetics of the coagulation of colloidal solutions. Zeitschriftfuer Physikalische Chemie, Zeitschriftfuer Physikalische Chemie 92, 129-168, 1917.

Su, W. G., Zhang, J., Feng, Z. C., Chen, T., Ying, P. L., and Li, C.: Surface phases of TiO_2 nanoparticles studied by UV Raman spectroscopy and FT-IR spectroscopy, J. Phys. Chem. C, 112, 7710-7716, https://doi.org/10.1021/jp7118422, 2008.

Truhlar, D. G., Hase, W. L., and Hynes, J. T.: Current Status Of Transition-State Theory, J. Phys. Chem., 87, 2664-2682, https://doi.org/10.1021/j150644a044, 1983.

Wigner, E.: On the Penetration of Potential Energy Barriers in Chemical Reactions, Z. Phys. Chem. Abt. B 19, 203-216, 1932.

Yousaf, K. E., and Peterson, K. A.: Optimized auxiliary basis sets for explicitly correlated methods, J. Chem. Phys., 129, https://doi.org/10.1063/1.3009271, 2008.

Zhao, Y., and Truhlar, D. G.: The M06 suite of density functionals for main group thermochemistry, thermochemical kinetics, noncovalent interactions, excited states, and transition elements: two new functionals and systematic testing of four M06-class functionals and 12 other functionals, Theor. Chem. Acc., 120, 215-241, https://doi.org/10.1007/s00214-007-0401-8, 2008.